Power-Flow-Based Secondary Control for Autonomous Droop-Controlled AC Nanogrids With Peer-to-Peer Energy Trading

CARLOS RONCERO-CLEMENTE[1], **EVA GONZÁLEZ-ROMERA**[1],
FERMÍN BARRERO-GONZÁLEZ[1], (Senior Member, IEEE),
MARÍA ISABEL MILANÉS-MONTERO[1], (Member, IEEE),
AND ENRIQUE ROMERO-CADAVAL[1], (Senior Member, IEEE)
Power Electrical and Electronic Systems Research Group, University of Extremadura, 06006 Badajoz, Spain

Corresponding author: Carlos Roncero-Clemente (carlosrc@unex.es)

ABSTRACT Regarding the control of micro- and nanogrids, LC- or LCL-filtered power inverters (acting as interfaces with distributed energy resources such as photovoltaic or wind) commonly perform as grid-forming or grid-supporting units to maintain both the frequency and voltage within pre-set standards. Nevertheless, these power inverters are assumed to be connected at the same point of common coupling directly or via radial feeders; thus, the voltage references are the same for each parallel power inverter, thus requiring a virtual impedance loop. In addition, classic power sharing techniques comply with their individual power rates, and circulating currents among distributed generators are not considered. Under these circumstances, energy trading among prosumers and peer-to-peer contracts is not feasible in autonomous AC micro- and nanogrid operations. This paper proposes a reformulated power flow problem, adapted to autonomous droop-controlled AC microgrids, to be used as a secondary control layer. The entire hierarchical control is implemented and experimentally validated in a laboratory-scale nanogrid with energy storage systems, photovoltaic generators and power converters. The obtained results demonstrate the proper performance of the proposed approach, with successful operation of primary and inner controllers.

INDEX TERMS Distributed power generation, energy storage, hierarchical systems, microgrids, power quality, renewable energy sources and smart grids.

I. INTRODUCTION

Microgrids (μGs) and nanogrids (nGs) are low-scale grids involving emerging technologies as modern power converters interfacing both distributed energy resources (most likely based on renewable sources) and energy storage systems (ESSs) [1], [2]. These distributed generators (DGs) are optimally coordinated by using information and communication infrastructures to supply electricity demand in an efficient and clean way (according to the Internet of Energy (IoE) concept [3]). Current microgrid deployment mostly arises from the goal of integrating DGs based on

The associate editor coordinating the review of this manuscript and approving it for publication was Giambattista Gruosso.

renewables to alleviate CO_2 emissions while reducing power transmission losses and costs, acting as a single controllable entity with respect to the main grid if needed (autonomous operation) [4]–[6].

μGs and nGs are less robust than bulk power systems against power mismatches between generation and consumption when they are islanded. At the same time, problems related to the reliability of μGs and nGs due to the interactions between electrical and communication networks have been widely analysed in the literature [7]. In this sense, hierarchical control arrangements are accepted as standard solutions, but there is a trade-off between the accurate performance of centralized approaches and the flexibility and resilience offered by distributed controls [2], [8]. At the

bottom level in hierarchical control, well-known droop functions (*P-f* and *Q-V* dependences) enable local regulation of the voltage RMS value (*V*) and frequency (*f*) in a μG/nG by means of distributed power inverters [9]. Thus, primary control aims to balance power mismatches at the expense of both *f* and *V* deviations within a range when a μG or nG operates autonomously. This first level also includes the inner current and voltage control loops. In an upper level, secondary control aims to cancel the *V* and *f* steady-state errors. This action is carried out by sending new reference power values back to the DGs once this controller has computed voltage and frequency measurements from different nodes of the μG [10]. Finally, the upper or third layer constitutes the tertiary control, which responds to power management issues and coordination between different μGs and/or the main grid. Tertiary control is performed at a central controller, which receives multiple data points (weather forecasts, energy prices, load profiles, ESS state of charge (SoC), efficiency metrics and possible smart contracts among stakeholders) to apply an optimization algorithm [8], [11].

The European Commission set up key targets for 2030, including 40% cuts in greenhouse gas emissions (from 1990 levels, although an increase to 55% has been recently proposed), increasing up to at least a 32% share of renewable energy and at least a 32.5% improvement in energy efficiency [12]. Thus, considerable renewable energy penetration and μG/nG configurations are expected during the next decade. At the same time, an evolution from classic consumers into so-called prosumers is crucial to accomplish this challenge. These prosumers are intended as μG/nG users that combine energy production and consumption, who sell or buy energy in a bidirectional way with other neighbouring prosumers. Concurrently, local energy trading has attracted interest from industry and academia. Nevertheless, most studies have dealt with energy trading between μGs and nGs. For instance, a convex optimization framework was developed for energy trading between islanded μGs in [13]. External interactions among interlinked μGs and their internal power sharing were also extensively analysed in [14]. In this work, the authors studied how the renewable generation surplus may be traded with other μGs lacking power supplies for mutual benefits. The authors in [15] addressed a flexible energy trade between peers, where excess energy was traded among local customers in three different paradigms. A more collaborative approach, such as existing mobility or house-renting platforms, was discussed in [16]. In this paper, energy producers and consumers participate in a local energy market to obtain benefits (peer-to-peer (P2P) approach). In [17], only photovoltaic (PV) prosumers are considered to build an energy sharing model that involves price-based demand responses and energy costs. These PV prosumers determine the energy price and schedule power generation. Furthermore, clustering strategies and virtual aggregation techniques demonstrates an energy cost reduction strategy among μG prosumers [18]. Hierarchical decision-making and game-theory approaches were formulated with similar

purposes in [19] and [20], respectively. Electrical vehicle (EV) impacts and possibilities have gained popularity among μG stakeholders. This issue must also be considered when analysing this kind of system in the presence of EVs [21].

Despite the fact that several works have focused on P2P energy trading in μGs or nGs [22], [23], the majority have been devoted to economic aspects and validated by computer simulations. There is a lack of studies exploring how DGs may track power references coming from P2P contracts together with hierarchical control in autonomous μGs or nGs. In particular, two suppositions are commonly found in the μG or nG control bibliography [2], [24].

- LC- or LCL-filtered power inverters interface distributed energy sources with μGs or nGs, making them behave as grid-forming or grid-supporting units [25] to maintain adequate *f* and *V* within the μG limits. However, they are assumed to be connected to the same point of common coupling (PCC) in a direct way or via radial feeders, together with the corresponding loads [26]. Under this premise, the output AC voltage reference is the same for each DG, while a virtual impedance loop is added to decouple the *P-f* and *Q-V* dependencies.
- Power sharing complies with individual power rates, thus avoiding circulating currents among DGs. In this case, possible energy trading supported by P2P contracts is frequently omitted in autonomous μG operations.

In addition, an updated and comprehensive review on secondary control architectures in AC μGs [27] indicated that this layer has to generate an additional term for droop control to restore *f* and *V* to the reference values after a certain time period. Frequency and voltage references are the same for each power inverter, as they are assumed to be located at the same PCC. Operating in this way, no power exchange is permitted among power converters; thus, collaborative P2P contracts are not feasible in autonomous μGs.

Nevertheless, prosumers, ESSs, PV-based DGs, EVs, etc. are connected to different load buses at different locations within a μG or nG. Thus, different power and voltage references for those units could allow circulating currents and collaborative P2P energy trading. As a consequence, power flow equations have to be reformulated to guarantee the technical feasibility of this approach to deal with the considered target. However, only a few studies have focused on the formulation of power flow equations within a μG, and they are typically used to analyse the μG behaviour rather than for control purposes [28], [29]. A strategy for autonomous μG secondary control consisting of a multiobjective function sought to reduce voltage errors in different buses in [30]. The multiobjective function, together with power flow equality constraints and three sets of inequality constraints, obtained the voltage regulation and minimum reactive circulating current. Nevertheless, no active power exchange among prosumers has been considered. Power quasi-average estimators for each load bus were considered in islanded μGs to regulate power

and frequency in a hierarchical approach in [31]. Estimators decentralized secondary control, preventing communication faults at the expense of computational burden.

As a summary of the state of the art related to the topic of this paper, it can be stated that the hierarchical control of μGs or nGs has been widely studied and continuously improved in the research literature. However, in previous works, energy interchange among μG/nG resources has often been avoided, as this is considered to imply unnecessary circulating currents. Moreover, a new paradigm in energy policies that encourages the presence of prosumers and the formalization of P2P energy trading among them introduces a new challenge to adapt classic hierarchical controls to multibus μG/nG prosumers that allow for energy interchanges among them. This adaptation requires the observance of power flow rules modified for islanded μGs controlled by droop-based grid-forming or grid-supporting units.

The main contributions of this work are highlighted as follows:

- A new secondary control approach based on a power flow algorithm with reformulated equations for a single-phase LCL filtered power inverter is developed. This secondary control approach makes P2P energy trading compatible among AC autonomous nG users since individual voltage and power references are provided.
- The proper performance of the secondary control [32] is experimentally verified in a residential autonomous AC nG at the laboratory scale. The obtained results demonstrate the proper operation of hierarchical control by means of the necessary control loops.

Section II explains each control layer from the hierarchical structure point of view, focusing on the proposed secondary controller for a nG, which is progressively revealed. Then, section III describes the case study and its main parameters. In addition, the required low-level controllers, inner current and voltage control loops, and DC-link voltage control loops are presented. The nG setup description and experimental results are presented and discussed in section IV. Finally, section V concludes the work.

II. NANOGRID CONTROL LAYERS

A hierarchical structure is adopted in this work due to the aforementioned reasons for controlling an autonomous nG. The upper (which is also the slowest) control layers constitutes the nG energy management systems (EMSs), which have crucial importance when a nG is connected to the main grid to ensure negotiation for improving nG self-consumption or for selling energy during high-price time periods. At the same time, it is important to consider that PV facilities must be widely exploited to reduce greenhouse emissions while improving autonomous performance. To address this issue, we consider that all PV power generators extract maximum power, except if the SoC and power demands are completely fulfilled. Given this situation, PV power curtailment

techniques must be used, such as changing the maximum power point (MPP) operation to a reference power point [33]. After these considerations, the tertiary control layer determines the active and reactive power references ($P^*_{G-TERTi}$ and $Q^*_{G-TERTi}$) in every bus, updating their values each hour for individual converters. Another assumption is that PV and ESS are linked to each other by means of a common power converter to the prosumer's load node i. At the same time, circulating reactive currents are not desired among different nG prosumers because higher losses and voltage drops would arise. In this sense, $P^*_{G-TERTi}(t)$ and $Q^*_{G-TERTi}(t)$ can be expressed as (1): (note that the study of the tertiary control layer is considered out of the scope of this work)

$$P^*_{G-TERTi}(t) = P_{Gi}(t) + P_{ESSi}(t)$$
$$Q^*_{G-TERTi}(t) = Q_{Di}(t) \qquad (1)$$

where $P_{Gi}(t)$ is the mean forecasted PV power and $P_{ESSi}(t)$ represents the mean scheduled ESS power (positive when discharging and negative when charging) during each hour. $Q_{Di}(t)$ is the mean forecasted reactive power drawn by the load per hour.

A. POWER-FLOW-BASED SECONDARY CONTROL IN THE NANOGRID

Once $P^*_{G-TERTi}(t)$ and $Q^*_{G-TERTi}(t)$ are solved hourly by the tertiary control layer, secondary control is responsible for calculating active and reactive power references, together with the voltage reference for each nG power inverter with a reduced time step. The secondary control target aims to restore f and V values within the nG if those values deviate from primary control in the case of power generation and demand mismatches. This secondary control layer presents a centralized architecture, including slow control loops and low-bandwidth communication systems. A one-minute time step is assumed for this control layer execution time. ESS power (P_{ESS0i}) is calculated by linearly interpolating two consecutive $P_{ESSi}(t)$ values. In the meantime, the generated and demanded active powers for each load bus i (P_{G0i} and P_{D0i}, respectively) are the measures of the previous minute and are applied to calculate the updated secondary control references, which will be different in each load bus, allowing for P2P energy trading among prosumers. These updated secondary control references are droop-controlled; therefore, robust matching with voltage references and a power flow algorithm is required. In this sense, a power flow algorithm formulation for autonomous AC nGs is developed to obtain both power and voltage references. The initial conditions for the power flow problem will be updated once a minute; hence, quasistatic behaviour is assumed for nGs during that period of time.

Several power flow algorithms for autonomous AC μGs and nGs are available from previous works [34] and are frequently used in the tertiary control layer instead of the secondary level. Some differences between this formulation and

the formulation for traditional power systems are summarized as follows:

- A slack bus is not available because no powerful generation capacity is available in any node, which would guarantee a fixed f in addition to compensating for power system losses. Nevertheless, new buses are present in the nG: PQ buses (intended as consumption and/or power production buses) and droop buses, which share the target of stabilizing f and V.
- The f parameter is unknown.
- Active and reactive power production are droop-controlled.

The following subsections describe the proposed power flow algorithm formulation as a secondary controller and how to perform the adequate transformation from the obtained references to references trackable by the primary controller.

1) SYSTEM MODELLING

A short-line model is assumed for the nG; thus, shunt admittance is disregarded. In this case, only the series impedance ($\vec{Z}_{ij}$) between buses i and j is taken into account (2):

$$\vec{Z}_{ij} = R_{ij} + X_{ij} = R_{ij} + 2\pi f L_{ij} \qquad (2)$$

where R_{ij}, X_{ij} and L_{ij} are the line resistance, line reactance and line inductance, respectively.

The active and reactive power demanded by prosumer loads (P_{D-SECi} and Q_{D-SECi}) depend on the RMS voltage (V_i) and f at load bus i. Their influence on the demanded power is different according to the nature of the load. A generalized model for the linear load is expressed in (3).

$$P_{D-SECi} = P_{D0i} \left(\frac{V_i}{V_n}\right)^{\alpha} \left[1 + k_{pf}\left(\frac{f - f_n}{f_n}\right)\right]$$
$$Q_{D-SECi} = Q_{D0i} \left(\frac{V_i}{V_n}\right)^{\beta} \left[1 + k_{qf}\left(\frac{f - f_n}{f_n}\right)\right]. \qquad (3)$$

V_n and f_n are the nominal RMS voltage and nominal frequency at load bus i, respectively, and Q_{D0i} is the measured previous minute value of the reactive power demanded by the load. Finally, α and β represent voltage exponents for active and reactive power, respectively, and k_{pf} and k_{qf} represent frequency slopes for active and reactive power, respectively. In the case of household loads, illustrative values from [35] are provided (Table 1).

TABLE 1. Exponents and Frequency Sensitive Factors.

Season	α	β	k_{pf}	K_{qf}
Summer	1.2	2.7	0.7	-2.3
Winter	1.7	2.6	1	-1.7

As previously mentioned, PQ buses do not control either V or f; thus, they can be modelled as load buses with the corresponding sign criterion. Nevertheless, DGs that regulate

V and f within a nG are droop-controlled (droop buses) and modelled as follows (4) for inductive lines:

$$P^*_{G-SECi} = P_{G0i} + \left[\frac{1}{m_p}(f_n - f)\right]$$
$$Q^*_{G-SECi} = Q_{G0i} + \left[\frac{1}{m_q}(V_n - V_i)\right] \qquad (4)$$

and (5) for resistive lines:

$$P^*_{G-SECi} = P_{G0i} + \left[\frac{1}{k_p}(V_n - V_i)\right]$$
$$Q^*_{G-SECi} = Q_{G0i} + \left[\frac{1}{k_q}(f - f_n)\right], \qquad (5)$$

with P^*_{G-SECi} and Q^*_{G-SECi} as active and reactive power references for the power inverter in droop buses (derived from the secondary controller) and m_p, m_q, k_p and k_q as droop coefficients. In our particular case, a method to select droop coefficients as a function of the ESS state of charge is selected [36].

2) PROPOSED POWER FLOW ALGORITHM

Assuming balanced voltage in the droop buses, the formulation of power flow equations for single-phase autonomous nGs is similar to that in classic power systems. The injected active and reactive powers (P_{SECi} and Q_{SECi}) into bus i are determined as (6):

$$\left.\begin{array}{c} P_{SECi} = P^*_{G-SECi} - P_{D-SECi} \\ = V^*_{SECi} \sum_{k=1}^{n} V^*_{SECk} Y_{ik} \cos(\delta^*_{SECi} - \delta^*_{SECk} - \gamma_{ik}) \\ Q_{SECi} = Q^*_{G-SECi} - Q_{D-SECi} \\ = V^*_{SECi} \sum_{k=1}^{n} V^*_{SECk} Y_{ik} \sin(\delta^*_{SECi} - \delta^*_{SECk} - \gamma_{ik}) \end{array}\right\} \quad (6)$$

where V^*_{SECi}, V^*_{SECk}, δ^*_{SECi} and δ^*_{SECk} are the RMS value and phase angle of the i-bus and k-bus reference voltages, respectively. Y_{ik} and γ_{ik} represent the magnitude and phase angle of the ik-element of the Y_{bus} admittance matrix.

In PQ buses, it is necessary to determine V^*_{SECi} and δ^*_{SECi}. However, P^*_{G-SECi}, Q^*_{G-SECi}, V^*_{SECi} and δ^*_{SECi} are the variables to be determined in a droop bus. If one of the droop buses is considered with null phase angle reference ($\delta^*_{SECi} = 0$), the same number of unknown variables and equations are derived (remembering that f must also be calculated). Thus, equations for solving both the PQ bus and droop bus are set as follows (equations (7) and (8), respectively) (variables with superscripts (*) are considered reference magnitudes):

$$\left.\begin{array}{c} 0 = P_{D-SECi} - P^*_{G-SECi} \\ +V^*_{SECi} \sum_{k=1}^{n} V^*_{SECk} Y_{ik} \cos(\delta^*_{SECi} - \delta^*_{SECk} - \gamma_{ik}) \\ 0 = Q_{D-SECi} - Q^*_{G-SECi} + \\ = V^*_{SECi} \sum_{k=1}^{n} V^*_{SECk} Y_{ik} \sin(\delta^*_{SECi} - \delta^*_{SECk} - \gamma_{ik}) \end{array}\right\} \quad (7)$$

$$\left.\begin{array}{c} 0 = P_{D-SECi} - P^*_{G-SECi} + \\ +V^*_{SECi} \sum_{k=1}^{n} V^*_{SECk} Y_{ik} \cos(\delta^*_{SECi} - \delta^*_{SECk} - \gamma_{ik}) \\ 0 = Q_{D-SECi} - Q^*_{G-SECi} + \\ = V^*_{SECi} \sum_{k=1}^{n} V^*_{SECk} Y_{ik} \sin(\delta^*_{SECi} - \delta^*_{SECk} - \gamma_{ik})) \\ 0 = P^*_{G-SECi} - P_{G0i} - \frac{1}{k_p}(V_n - V^*_{SECi}) \\ 0 = Q^*_{G-SECi} - Q_{G0i} - \frac{1}{k_q}(f - f_n) \end{array}\right\} \quad (8)$$

Resistive line models and the trust-region Newton method are considered to solve the formulated problem [28]. Thus, the proposed algorithm, once solved, determines P^*_{G-SECi}, Q^*_{G-SECi}, V^*_{SECi} and δ^*_{SECi} in each prosumer's load bus, accomplishing initial agreements and power flow, voltage and frequency control within the nG. As an example, Fig. 1 illustrates the previous references and their location in a two-droop bus-based nG.
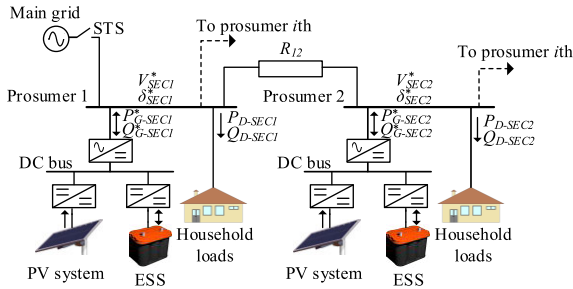

FIGURE 1. Secondary control references and their locations in a two-droop bus-based autonomous AC nG.

B. TRANSFORMATION TO REFERENCES COMPATIBLE WITH PRIMARY CONTROL

The equivalent circuit of the LCL-filtered single-phase power inverter located in any prosumer's load bus i is represented in Fig. 2. Inductances $L_{1,i}$, $L_{2,i}$ and capacitance $C_{f,i}$ correspond to the converter and load side inductances and the filter capacitor.
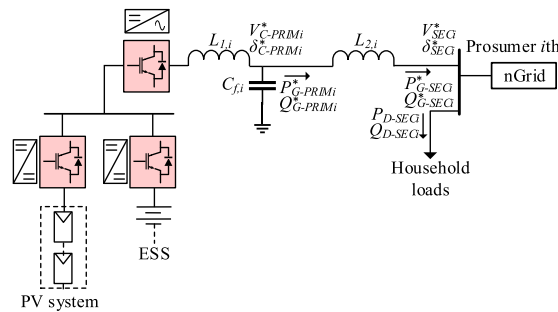

FIGURE 2. Primary control references in the output filter of power inverter I in autonomous AC nG.

After obtaining P^*_{G-SECi}, Q^*_{G-SECi}, V^*_{SECi} and δ^*_{SECi} the secondary controller, primary control will dynamically regulate V and f at the power inverter side.

The capacitor RMS reference voltage ($V^*_{C-PRIMi}$) and its phase angle ($\delta^*_{C-PRIMi}$), jointly the active and reactive power references ($P^*_{G-PRIMi}$ and $Q^*_{G-PRIMi}$) that can be tracked by primary control, are located at the input terminal of $L_{2,i}$. These values can be calculated as (9):

$$
\left.
\begin{aligned}
S_{G-SECi} &= v_{SECi}\overline{i_{L2}} \\
&= v_{SECi}\frac{\overline{v_{C-PRIMi}-v_{SECi}}}{-j2\pi f L_{2,i}} \rightarrow V^*_{C-PRIMi}, \delta^*_{C-PRIMi} \\
S_{G-PRIMi} &= v_{C-PRIMi}\overline{i_{L2}} \\
&= v_{C-PRIMi}\frac{\overline{v_{C-PRIMi}-v_{SECi}}}{-j2\pi f L_{2,i}} \rightarrow P^*_{G-PRIMi}, Q^*_{G-PRIMi}
\end{aligned}
\right\} \quad (9)
$$

where $\overline{i_{L2}}$ is the complex conjugate of the current in $L_{2,i}$. It is important to note that equation (9) is solved locally.

Then, droop control terms are included to correct the previous references in the case of power generation and power demand mismatches. As inductive impedance is predominant between $C_{f,i}$ and bus i, the droop condition is given by (4). The set of equations (10) determines the instantaneous voltage reference in filter capacitor $C_{f,i}$ (v^*_{Ci}) to be tracked through the inner voltage and current controllers:

$$
\left.
\begin{aligned}
V^*_{Ci} &= V^*_{C-PRIMi} + m_q\left(Q^*_{G-PRIMi} - Q_i\right) \\
\theta^*_{Ci} &= \delta^*_{C-PRIMi} + {}^{2\pi}/_s\left[f_n + \right. \\
&\left. + m_p\left(P^*_{G-PRIMi} - P_i\right)\right] \\
v^*_{Ci} &= \sqrt{2}V^*_{Ci}\sin\left(\theta^*_{Ci}\right)
\end{aligned}
\right\}, \quad (10)
$$

with P_i and Q_i as the active and reactive power measures in $L_{2,i}$.

Droop coefficients used in secondary and primary controllers are calculated by considering the maximum value of V and f deviations ($\pm 7\%$ of rated value and ± 1 Hz, respectively) from the Spanish standard [37] and the available power capacity in each DG (PV production, ESS maximum power and its SoC). At the same time, droop rules are applied in two stages. First, the secondary control level considers resistive lines (5), and second, the primary control level considers inductive lines (4). Thus, decoupled active/reactive power and frequency/voltage are guaranteed, avoiding the use of a virtual impedance loop.

III. CASE STUDY

Two droop buses including two prosumer installations are considered to validate the proper performance of the secondary controller as an example of a simplified autonomous AC nG. Each facility involves a PV generation system, an ESS and household loads. The two buses are connected via a typical low-voltage distribution two-wire cable ($R_{1,2}$) with a 6 mm^2 cross-section that is 20 m long.

Fig. 3 represents the schematic of the nG, where the variables and measurements required in the primary closed-loop controllers are highlighted in red. The dynamics of PV system study are out of the scope of this work, and it is considered to be working at MPP for both prosumers to maximize the exploitation of this DG. Thus, the PV array and its associated
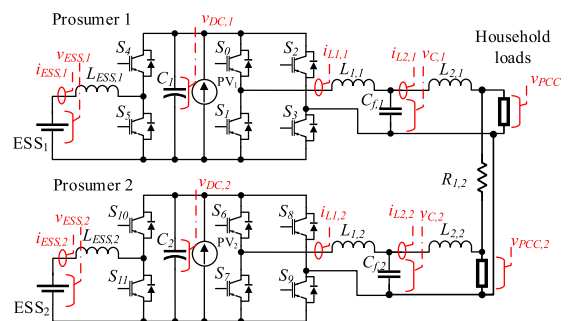

FIGURE 3. Autonomous AC nG with a two prosumer scheme.

power inverter are replaced by a DC controlled current source (PV$_i$) that injects the PV power directly into the DC link. The ESS$_i$ interface consists of a half-bridge bidirectional buck-boost DC-DC power converter (switches S_4 and S_5 and S_{10} and S_{11} for prosumers 1 and 2, respectively). A first-order filter (inductance $L_{ESS,i}$) is chosen for each ESS, taking into account the internal resistance $R_{L-ESS,i}$ in the control stage for higher accuracy. In addition, traditional full-bridge power inverters connect both distributed generators to the load bus of each prosumer via LCL filters. The connected load in each bus changes during autonomous operation.

Table 2 summarizes the values of the passive elements and the nG specifications. The laboratory nG was assembled at a 1:2 scale. Table 2 also discloses the droop values used in the primary control as a function of the values used in secondary control, considering the different aforementioned relationships regarding the resistive nature of the lines between prosumers (in secondary control) and the inductive nature of the power inverter filter (in primary control).

TABLE 2. Nanogrid Experimental Parameters.

	Parameter and unit	Value
PASSIVE ELEMENTS	ESS filter resistance, $R_{ESS,i}$ (Ω)	0.16
	ESS filter inductance, $L_{ESS,i}$ (mH)	8
	DC-link capacitor, C_i (mF)	1.1
	Converter side filter inductance, $L_{1,i}$ (mH)	3.6
	Capacitor filter, $C_{f,i}$ (μF)	2
	Load bus i side filter inductance, $L_{2,i}$ (mH)	4.2
	Initial and final resistive load (Ω)	33.5-23.5
	Initial and final inductive load (H)	0.27-0.23
nG SPECIFICATIONS	Nominal ESS voltage (V)	48
	Nominal DC-link voltage (V)	270
	Nominal AC voltage in prosumer bus (V)	115
	Nominal frequency (Hz)	50
DROOP CONSTANTS (PRIMARY CONTROL)	$m_{p1}= k_{q1}$ (Hz/W, Hz/VAr)	3.3e^{-5}
	$m_{q1}= k_{p1}/100$ (V/VAr, V/W)	1.1e^{-5}
	$m_{p2}= k_{q2}$ (Hz/W, Hz/VAr)	3.1e^{-5}
	$m_{q2}= k_{p2}/100$ (V/VAr, V/W)	2.5e^{-5}

Table 3 shows the previous and new power demand forecasts (P_{D-SECi} and Q_{D-SECi}), as well as the power and voltage references (P^*_{G-SECi}, Q^*_{G-SECi}, V^*_{SECi} and δ^*_{SECi}) derived from the secondary control for each prosumer. To formulate the power flow problem, a constant power load model was chosen with null exponents and sensitive factors according to (3). Power references are different than the power demanded by each prosumer. This situation is produced due to the droop constants employed by the secondary control for power sharing (8), in accordance with the energy resources available at each prosumer facility.

Finally, the values $V^*_{C-PRIMi}$, $\delta^*_{C-PRIMi}$, $P^*_{G-PRIMi}$ and $Q^*_{G-PRIMi}$ calculated with (9) are also given.

Fig. 4 represents the block diagram including the nG secondary and primary controls. Some stages of the control have already been detailed. At the same time, the ESS is

TABLE 3. Previous and New Power and Voltage References from Secondary Control.

| Prosumer 1	Previous value	New value	Prosumer 2	Previous value	New value
P_{D-SEC1}	153.78	321.77	P_{D-SEC2}	241	241
Q_{D-SEC1}	117	117	Q_{D-SEC2}	38.91	66.03
P^*_{G-SEC1}	275.62	312.29	P^*_{G-SEC2}	119.237	250.478
Q^*_{G-SEC1}	117	117	Q^*_{G-SEC2}	38.91	66.03
V^*_{SEC1}	115.0568	114.9956	V^*_{SEC2}	114.987	115.001
δ^*_{SEC1}	0	0	δ^*_{SEC2}	0	0
$P^*_{G-PRIM1}$	279.003	316.497	$P^*_{G-PRIM2}$	119.832	253.015
$Q^*_{G-PRIM1}$	125.511	127.569	$Q^*_{G-PRIM2}$	40.405	72.406
$V^*_{C-PRIM1}$	117.559	117.668	$V^*_{C-PRIM2}$	115.936	116.832
δ^*_{PRIM1}	0.0213	0.0247	δ^*_{PRIM2}	0.0098	0.021
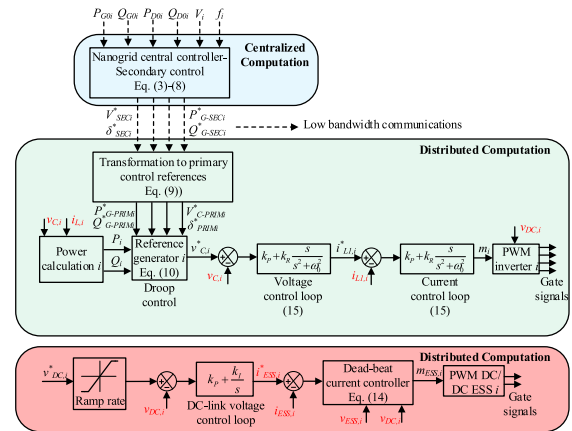
FIGURE 4. General block diagram of the nG control.

responsible for assuring the reference value of the DC-link voltage (v^*_{DCi}) during the operation, and the inner control loops have to provide accurate tracking of the voltage reference (v^*_{Ci}). The following subsection describes their study, design and tuning procedure.

A. DC-LINK VOLTAGE CONTROLLER AND POWER INVERTER INNER CONTROL LOOP DESIGN

The challenge in designing a DC-link bus voltage controller in a single-phase power inverter involves two main issues: 1) voltage variations resulting from sudden steps of the active power flow and 2) the inherent low-frequency pulsation from the single-phase power that fluctuates at double the nominal frequency [38]. Furthermore, the presence of these two issues can be transferred to the measurement system closing a control loop, thus deriving inaccurate reference signals.

Thus, more distorted electrical variables are expected, for example, in the output current. In addition, these highlighted problems unfortunately have a higher impact on autonomous μGs and nGs, which are less robust than classic power systems. The control target for the DC-link controller can be

listed as follows: 1) $v_{DC,i}$ must track the reference $v_{DC,i}^*$ with zero steady-state error, 2) DC-link voltage variations have to be dampened after step changes in AC power and 3) output current has to fulfil the most demanding grid codes.

Several control approaches deal with the DC-link voltage loop, and most of them are based on PI regulators [39]. A methodology for designing and tuning an adaptive PI controller aiming to optimize the previously listed control targets was proposed in [40]. Fig. 5 a) depicts a block diagram of the DC-link voltage control, where several assumptions were considered for our system.

a)

b)
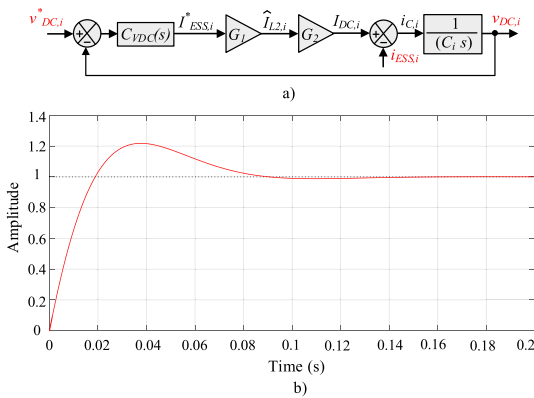
FIGURE 5. a) Simplified model of the DC-link voltage control and b) unity step-response for a dynamic DC-link voltage model with selected control parameters.

This modelling approach considers that the DC-link voltage control loop is sufficiently slow in comparison with the AC current and voltage control loops. In addition, nonlinearities and losses in both the ESS$_i$ bidirectional buck-boost DC-DC power converter and the full-bridge power inverter are omitted. At the same time, the ESS$_i$ power converter is in response to regulating the DC-link voltage, and null PV production is included (i.e., during night operation).

Expressions for $P_{G-PRIMi}$, DC-link handle power ($P_{DC,i}$) and power injected by/demanded from the ESS ($P_{ESS,i}$) are given as (11):

$$\left.\begin{array}{l} P_{G-PRIMi}=\dfrac{\hat{V}_{Ci}\hat{I}_{L2,i}}{2} \\ P_{DC,i} = v_{DC,i}I_{DC,i} \\ P_{ESS,i} = v_{ESS,i}I_{ESS,i} \\ P_{G-PRIMi} = P_{DC,i} = P_{ESS,i} \end{array}\right\} \quad (11)$$

where $\hat{V}_{Ci}$ and $\hat{I}_{L2,i}$ are the peak values of the filter capacitor voltage and load bus side inductor current, respectively. $I_{DC,i}$, and $I_{ESS,i}$ correspond to the DC and ESS averages, respectively. By rearranging (11), gains (G_1 and G_2) represented in Fig. 5 a) can be determined (12).

$$\left.\begin{array}{l} \hat{I}_{L2,i} = \dfrac{2v_{ESS,i}}{\hat{V}_{Ci}}I_{ESS,i} = G_1 I_{ESS,i} \\ I_{DC,i} = \dfrac{V_{Ci}}{2v_{DC,i}}\hat{I}_{L2,i} = G_2\hat{I}_{L2,i} \end{array}\right\} . \quad (12)$$

Thus, the characteristic equation associated with the considered model is $s^2 + \left(G_1 G_2 K_p^{DC}\Big/C_i\right)s + G_1 G_2 K_{pi}^{DC}\Big/C_i = 0$,

where K_p^{DC} and K_{pi}^{DC} are the proportional and integral gains of the DC-link voltage PI controller ($C_{VDC}(s)$). The characteristic equation on its canonical form is expressed as $s^2 + 2\xi\omega_n s + \omega_n^2 = 0$, with ξ and ω_n representing the damping ratio and the natural frequency, respectively. Once ξ and ω_n are chosen, the PI constant values for the DC-link controller K_p^{DC} and K_{pi}^{DC} are calculated as (13).

$$K_p^{DC} = \frac{2C_i\xi\omega_n}{G_1 G_2} \text{ and } K_i^{DC} = \frac{C_i\omega_n^2}{G_1 G_2}. \quad (13)$$

DC-link voltage control loop stability is guaranteed if $K_p^{DC} > 0$ and $K_{pi}^{DC} > 0$. By setting the damping ratio to 0.7 and ω_n to 82.715 rad/s, a good trade-off between DC-link voltage variations and output current quality is achieved. In addition, the initial K_p^{DC} and K_{pi}^{DC} values are refined by adjusting the unit step response characteristics of the dynamic system. Fig. 5b) plots the closed-loop unity step response with $K_p^{DC} = 0.5$ and $K_{pi}^{DC} = 22$.

The PI controller outputs the ESS average reference current ($I_{ESS,i}^*$), taking a positive value for discharging and a negative value for charging. The duty cycle ($m_{ESS,i}$) calculation for the bidirectional buck-boost DC-DC power converter is developed by a deadbeat current controller. Assuming that $i_{ESS,i}$ is constant during the switching period (T_{SW}) and solving the circuit presented in Fig. 3, the resulting equation for calculating $m_{ESS,i}$ is (14):

$$m_{ESS,i} = \left(v_{ESS,i} - i_{ESS,i}R_{L-ESS,i} - -L_{ESS,i}\frac{I_{ESS,i}^* - i_{ESS,i}}{T_{sw}}\right)\frac{1}{v_{DC,i}}. \quad (14)$$

Note that the internal resistance of the magnetic component ($R_{L-ESS,i}$) is considered for higher accuracy during nG operation.
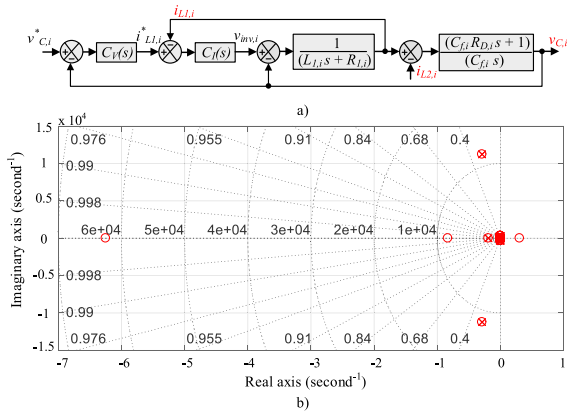
B. POWER INVERTER INNER CONTROL LOOPS
Once v_{Ci}^* is obtained from the droop controller (10), the power inverter inner loops have to accurately derive the modulating signal $i(m_i)$ to properly generate the gate signals with a pulse-width modulation (PWM) technique. The considered structure for controlling v_{Ci}^* is in the form of dual inner loops in a cascade: an outer loop for that voltage and the other loop for the current $i_{L1,i}^*$. For simplicity and reduced computational burden, proportional-resonant (PR) regulators are chosen for the voltage and current control loops. The reasons arise from the operation on the stationary α-β to avoid d-q rotational reference frame transformation. In addition, these regulators do not involve any plant parameter in the feedback loop.

The transfer functions of the voltage ($C_V(s)$) and current ($C_I(s)$) PR controllers are given by (15):

$$\left.\begin{array}{l} C_V(s) = K_{P-V} + K_{R-V}\dfrac{s}{s^2+\omega_0^2} \\ C_I(s) = K_{P-I} + K_{R-I}\dfrac{s}{s^2+\omega_0^2} \end{array}\right\} \quad (15)$$

where K_{P-V}, K_{P-I}, K_{R-V}, and K_{R-I} are the proportional gain terms and the resonant gain terms of $C_V(s)$ and ($C_S(s)$). ω_0 is the resonant frequency ($2\pi 50$ rad/s in this case).

To analyse the closed loop stability and to select the gain values, the model of the power inverter inner loops is obtained and represented in Fig. 6a). A damping resistor ($R_{D,i}$) is considered to reduce the selectivity of the third-order filter.

FIGURE 6. a) Block diagram of the power inverter inner control loop. b) Pole and zero location of the closed-loop system.

The closed-loop transfer function including the inner loops is derived from the block diagram in Fig. 6a) and expressed as (16):

$$V_{C,i} = \frac{C_V C_I Z_{Ci}}{Z_{Ci} + Z_{Li} + C_I + C_V C_I Z_{Ci}} V^*_{C,i}$$
$$- \frac{Z_{Ci}(Z_{Li} + C_I)}{Z_{Ci} + Z_{Li} + C_I + C_V C_I Z_{Ci}} i_{L2,i} \quad (16)$$

In (16), $Z_{Li}(s) = L_{1,i}s + R_{1,i}$ and $Z_{Ci}(s) = (C_{f,i}R_{D,i}s + 1)/sC_{f,i}$ (argument (s) of the Laplace transform is omitted to simplify). A common and simple tuning method consists of selecting K_P by means of the phase margin criterion and establishing the crossover frequency (f_c). Then, K_R is added in parallel, assuring that the resonant frequency is lower enough than f_c to assure stability. The selection of K_P must provide an adequate trade-off between transient response and phase margin.

In the case study, the poles and zero locations with $K_{P-V} = 0.001$, $K_{P-I} = 20$, $K_{R-V} = 100$, and $K_{R-I} = 2000$ are plotted in Fig. 6b). All poles are near-cancelling with their pairs or located at the left half-plane, and therefore, the closed loop transfer function is stable.

IV. EXPERIMENTAL VERIFICATION

An experimental prototype at the laboratory scale of an autonomous AC nG (see Table 2) was assembled and tested to further validate the proposed secondary controller along the primary and inner controls (Fig. 7). Both the bidirectional buck-boost DC-DC power converter and the power inverters are based on Semiteach IGBT power modules made by Semikron. Each branch consists of a SKM50GB12T4 branch module, driven by a SKHI22A board. The measurement stage is equipped with an LA55/SP1 sensor for measuring the
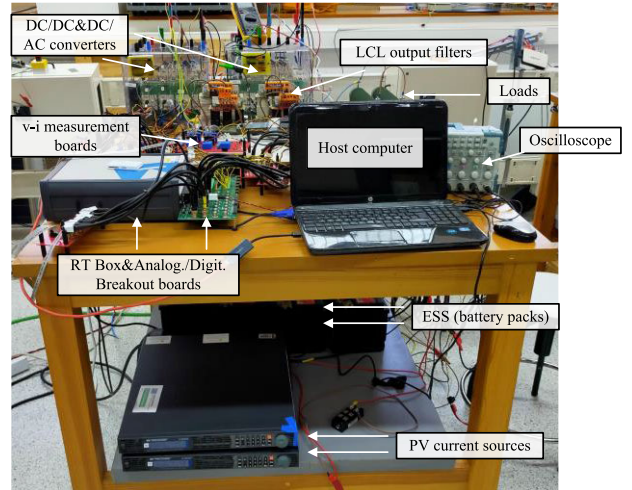
FIGURE 7. Experimental autonomous AC nanogrid setup at the laboratory scale.

corresponding currents and an LV-25-P sensor for the voltages, both made by LEM. These sensors perform with high precision, good linearity and low common mode disturbance power, and measurement stages are designed with a high level of modularity to be able to further add more DGs to the nG buses.

The control unit is an RT Box 1 from Plexim, which is used as a rapid prototype controller and equipped with analogue and digital breakout boards. This controller operates a Xilinx Zynq Z-7030 system-on-chip that embeds two CPU cores on an FPGA. The secondary controller was implemented in a script running in a host computer with MATLAB/Simulink, and PLECS Blockset software was used for the primary controllers running at 10 kHz.

The ESS battery pack for each prosumer is composed of 4 serial-12 V batteries. The PV power production is emulated with BK XLN60026 DC power supplies. All measurements were made by a Tektronix TPS2024B digital oscilloscope, Tektronix P5100A voltage probes and A622 current probes.

A. EXPERIMENTAL RESULTS

This subsection shows the main experimental waveforms obtained during nG operation with the specifications given in Table 2. For an easier understanding, Table 4 summarizes different events and time operation sequences from the beginning.

Fig. 8 shows the DC-link voltage evolution in prosumers 1 and 2 (Fig. 8 a) and b), respectively) during the nG operation test. A relay connects ESS i to the corresponding bidirectional buck-boost DC-DC power converter i; thus, DC link i starts at voltage ESS i (approximately 48 V, as shown during interval a). This initial voltage is transferred to DC-link capacitors C_1 and C_2 through antiparallel diodes of switches S_4 and S_{10} (see Fig. 3).

Then, the control and switching of the bidirectional buck-boost DC-DC power converter i to precharge DC link i and

**TABLE 4.** Events and Time Operation Sequences of Experimental Test.

| Event	Description
a	ESSs are connected to the corresponding DC-link i
b	Pre-charge and DC-link i stabilization with ESS converter i
c	Inverter 1 operation
d	Inverter 2 operation
e	PV$_1$ system operation
f	PV$_2$ system operation
	Drop control activation (no effects are observed as generation=consumption)
g	Load change
h	Updated references from secondary control
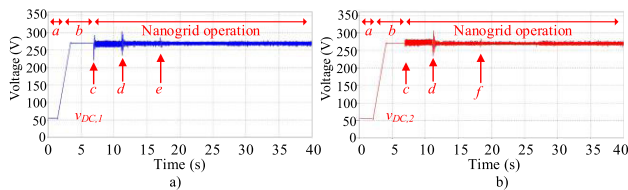
FIGURE 8. DC-link voltage ($v_{DC,i}$) evolution during nG operation. a) Prosumer 1. b) Prosumer 2.

to reach $v_{DC,i}^*$ (equal to 270 V) from the corresponding ESS_i are enabled (initial time in interval *b*). A ramp rate control to smooth the reference steps is implemented for this precharging process to reduce the ESS stress, thus avoiding undesired voltage overshoots. Once v_{dc1} and v_{dc2} show a stable voltage equal to 270 V (as each time interval *b* demonstrates in Fig. 8a) and b)), the control and switching of inverters 1 and 2 are activated to supply the load. The starting operation for each inverter produces a slight spike, but the voltage value is maintained very close to the reference. These minor spikes are noted at events *c* and *d* for inverters 1 and 2, respectively. Currently, AC nanogrid supplies loads by means of stored energy with high DC-link stability. Then, PV$_1$ and PV$_2$ systems start to inject power into the corresponding DC-link (starting PV$_1$ and PV$_2$ operations correspond to events *e* and *f*, respectively).

ESS currents ($i_{ESS,i}$) also reflect the same events. Fig. 9a) and b) depicts $i_{ESS,1}$ and $i_{ESS,2}$, respectively. These subfigures illustrate the ESS currents during the whole nG test. The $i_{ESS,1}$ and $i_{ESS,2}$ demanded during time interval *b* show a ramp trend that matches the programmed DC-link precharging function. Once v_{dc1} and v_{dc2} reach the reference voltage, $i_{ESS,1}$ and $i_{ESS,2}$ drop to zero, as expected (at the end of interval *b*). Then, the activation of inverters increases the values of $i_{ESS,1}$ and $i_{ESS,2}$ to supply the loads. Within interval *c*, only inverter 1 supplies the total load. $i_{ESS,1}$ in interval *c* is approximately 16 A at the steady state (measured $P_{ESS,1}$ was approximately 700 W). This value is higher than P_{load} due to the power conversion loss compensation by the ESS,
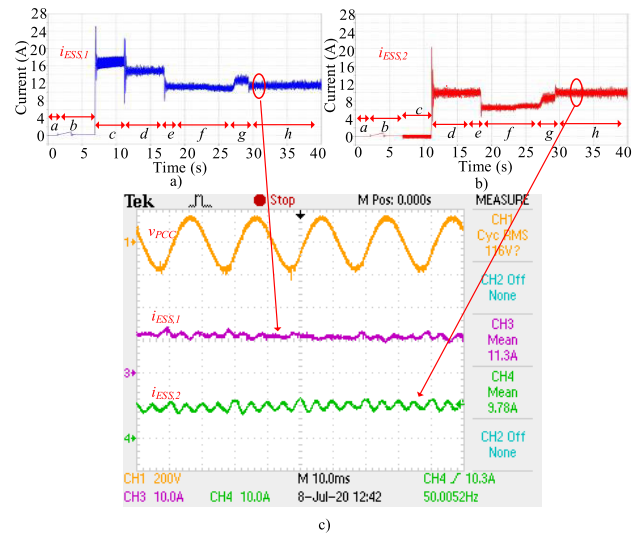

FIGURE 9. ESS current ($i_{ESS,i}$) evolution during nG operation. a) Prosumer 1 ($i_{ESS,1}$). b) Prosumer 2 ($i_{ESS,2}$). c) steady $i_{ESS,1}$ and $i_{ESS,2}$ waveforms and v_{PCC}.
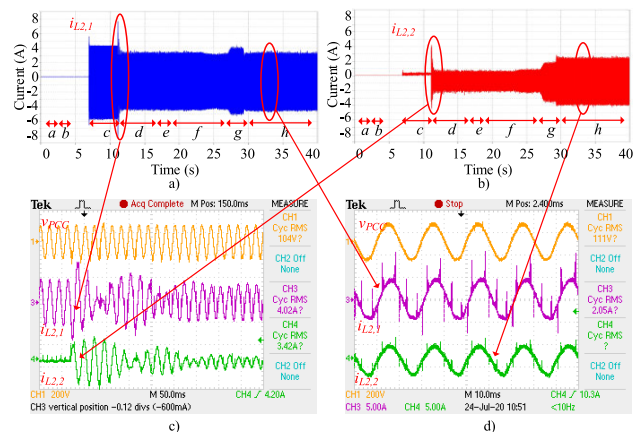
FIGURE 10. AC currents ($i_{L2,i}$). a) Evolution during nG operation for prosumer 1 ($i_{L2,1}$) and b) for prosumer 2 ($i_{L2,2}$). c) Transient response after power inverter 2 starts to operate. d) Steady $i_{L2,1}$ and $i_{L2,2}$ waveforms with v_{PCC}.

as expected. Once inverter 2 starts its operation, $i_{ESS,1}$ and $i_{ESS,2}$ are 13 A and 9 A, respectively (during time interval *d*). In this moment, initial set-points in each prosumer inverter i ($V_{C-PRIMi}^*$, $\delta_{C-PRIMi}^*$, $P_{G-PRIMi}^*$ and $Q_{G-PRIMi}^*$) are accomplished. Later, PV systems 1 and 2 (assumed to operate at MPP) contribute to the total energy production with 135 W each, and the demanded current from ESS 1 and 2 is reduced accordingly (events *e* and *f*, respectively).

Time interval *g* shows the load change at the AC side. In this case, a new power sharing is straightforwardly produced due to the primary droop controls (v_{Ci}^* has changed according to (10)). As droop constants m_{p1} and m_{p2} have similar values, a similar generation power increase is assumed by each prosumer. Secondary control references are updated at the end of the nG operation (time interval *h*).
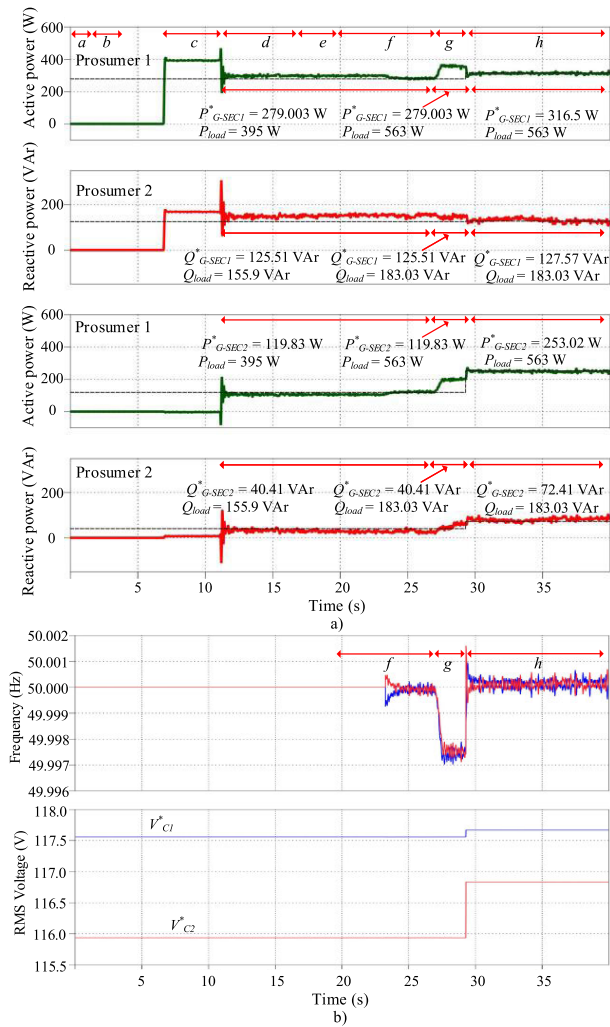
FIGURE 11. a) Evolution of active and reactive generated power, from top to bottom: P_1, Q_1, P_2 and Q_2. b) Frequency (top) and reference RMS voltage (bottom) at the output filter capacitors in each prosumer.

Details of the $i_{ESS,1}$ and $i_{ESS,2}$ waveforms are represented in Fig. 9c) together with the AC nG voltage at the PCC (v_{pcc}) in the steady state at the end of the nG operation. $i_{ESS,1}$ and $i_{ESS,2}$ ripples are under the design specifications.

Fig 10 shows the nG side output currents (AC side). Subfigures 10a) and 10b) depict $i_{L2,1}$ and $i_{L2,2}$, respectively, during the whole nG operation and testing, and the same events ($a − h$) are also highlighted there. Soft current spikes appear during the beginning of operation of each power inverter, but they are totally acceptable and safe (start of events c and d). Note that during time interval c, only prosumer 1 supplies the full load, and the initial power and voltage references are met in time interval d.

Detailed transient waveforms of $i_{L2,1}$ and $i_{L2,2}$ are shown in Fig. 10 c), which represent the time that power inverter 2 starts to switch and the initial power sharing is established according to initial references ($V^*_{C−PRIMi}$, $\delta^*_{C−PRIMi}$, $P^*_{G−PRIMi}$ and $Q^*_{G−PRIMi}$). This transient process takes

approximately 6-7 fundamental cycles, and the overshoot currents are approximately 20% of the nominal current. During this transient process, the AC nG voltage (v_{PCC}) at the PCC is quite stable, demonstrating the robustness of the system. Finally, Fig. 10 d) shows $i_{L2,1}$ and $i_{L2,2}$, together with v_{PCC} during the steady state at the end of the test (second load conditions and updated references). The measured total harmonic distortion of the output currents is below 3%.

Fig. 11 represents, from top to bottom, the measured active and reactive powers (P_i and Q_i), frequency and RMS voltage references (V^*_{C1} and V^*_{C2}) in both prosumer inverters. Once again, time events a to h are represented.

Active and reactive power are computed from the measured voltage in the corresponding filter capacitor and L_2 inductances (load sides). Active and reactive power references determined by primary control $P^*_{G−PRIMi}$ and $Q^*_{G−PRIMi}$ are also represented by dashed lines, whose values are properly tracked with the exception of interval g. In that period, the load changes, but the secondary control does not update the new references yet; thus, primary droop controls produce the new power sharing and the frequency drop deviation accordingly (see Fig. 11 b) top). In Fig. 11, P_{load} and Q_{load} are the sum of the active and reactive power demanded by both prosumers. It is thus verified that in any time interval, the sum of $P^*_{G−PRIM1}+P^*_{G−PRIM2}$ and $Q^*_{G−PRIM1}+Q^*_{G−PRIM2}$ are equal to P_{load} and Q_{load}, respectively.

V. CONCLUSION

P2P energy trading and contracts among nG users are crucial issues in the current electric energy scenario. The proposed secondary control approach for AC μG and nG accomplishes this functionality through a reformulated power-flow-based secondary controller in a hierarchical structure.

The power and voltage references obtained allow energy interchange and energy sharing between peers during autonomous operation. In addition, voltage and frequency control are properly controlled via droop rules together with the power flow between prosumers, as different power and voltage references are calculated in each prosumer's bus. The experiments demonstrate and validate the proper performance of the whole hierarchical control system. As a final conclusion, it can be stated that this control outperforms those that are common in the literature in which power sharing among prosumers obeys their energy rating, and circulating energy among them is usually avoided and hence allows for increased usability.

Future works will include research on the grid-connected case and the seamless transition between the on-grid and off-grid states, the inclusion of ancillary services, and the study of management strategies, including peer-to-peer transactions in the tertiary control layer.

REFERENCES

[1] N. Pogaku, M. Prodanovic, and T. C. Green, "Modeling, analysis and testing of autonomous operation of an inverter-based microgrid," *IEEE Trans. Power Electron.*, vol. 22, no. 2, pp. 613–625, Mar. 2007, doi: 10.1109/TPEL.2006.890003.

[2] J. M. Guerrero, J. C. Vasquez, J. Matas, L. G. de Vicuna, and M. Castilla, "Hierarchical control of droop-controlled AC and DC microgrids—A general approach toward standardization," *IEEE Trans. Ind. Electron.*, vol. 58, no. 1, pp. 158–172, Jan. 2011, doi: 10.1109/TIE.2010.2066534.

[3] H. Shahinzadeh, J. Moradi, G. B. Gharehpetian, H. Nafisi, and M. Abedi, "Internet of energy (IoE) in smart power systems," in *Proc. 5th Conf. Knowl. Based Eng. Innov. (KBEI)*, Tehran, Iran, Feb. 2019, pp. 627–636.

[4] Q. Shafiee, J. M. Guerrero, and J. C. Vasquez, "Distributed secondary control for islanded microgrids—A novel approach," *IEEE Trans. Power Electron.*, vol. 29, no. 2, pp. 1018–1031, Feb. 2014, doi: 10.1109/TPEL.2013.2259506.

[5] S. Parhizi, H. Lotfi, A. Khodaei, and S. Bahramirad, "State of the art in research on microgrids: A review," *IEEE Access*, vol. 3, pp. 890–925, 2015, doi: 10.1109/ACCESS.2015.2443119.

[6] M. Ahmed, L. Meegahapola, A. Vahidnia, and M. Datta, "Stability and control aspects of microgrid Architectures–A comprehensive review," *IEEE Access*, vol. 8, pp. 144730–144766, 2020, doi: 10.1109/ACCESS.2020.3014977.

[7] I. A. Tøndel, J. Foros, S. S. Kilskar, P. Hokstad, and M. G. Jaatun, "Interdependencies and reliability in the combined ICT and power system: An overview of current research," *Appl. Comput. Informat.*, vol. 14, no. 1, pp. 17–27, Jan. 2018.

[8] K. Mahmud, A. K. Sahoo, J. Ravishankar, and Z. Y. Dong, "Coordinated multilayer control for energy management of grid-connected AC microgrids," *IEEE Trans. Ind. Appl.*, vol. 55, no. 6, pp. 7071–7081, Nov. 2019, doi: 10.1109/TIA.2019.2931490.

[9] X. Meng, J. Liu, and Z. Liu, "A generalized droop control for grid-supporting inverter based on comparison between traditional droop control and virtual synchronous generator control," *IEEE Trans. Power Electron.*, vol. 34, no. 6, pp. 5416–5438, Jun. 2019, doi: 10.1109/TPEL.2018.2868722.

[10] E. Espina, J. Llanos, C. Burgos-Mellado, R. Cardenas-Dobson, M. Martinez-Gomez, and D. Saez, "Distributed control strategies for microgrids: An overview," *IEEE Access*, vol. 8, pp. 193412–193448, 2020, doi: 10.1109/ACCESS.2020.3032378.

[11] L. Meng, F. Tang, M. Savaghebi, J. C. Vasquez, and J. M. Guerrero, "Tertiary control of voltage unbalance compensation for optimal power quality in islanded microgrids," *IEEE Trans. Energy Convers.*, vol. 29, no. 4, pp. 802–815, Dec. 2014, doi: 10.1109/TEC.2014.2363687.

[12] European Commission, Brussels, Belgium. *2030 Climate & Energy Framework*. Accessed: Nov. 24, 2020. [Online]. Available: https://ec.europa.eu/clima/policies/strategies/2030_en#tab-0-0

[13] D. Gregoratti and J. Matamoros, "Distributed energy trading: The multiple-microgrid case," *IEEE Trans. Ind. Electron.*, vol. 62, no. 4, pp. 2551–2559, Apr. 2015, doi: 10.1109/TIE.2014.2352592.

[14] H. Wang and J. Huang, "Incentivizing energy trading for interconnected microgrids," *IEEE Trans. Smart Grid*, vol. 9, no. 4, pp. 2647–2657, Jul. 2018, doi: 10.1109/TSG.2016.2614988.

[15] C. Long, J. Wu, C. Zhang, L. Thomas, M. Cheng, and N. Jenkins, "Peer-to-peer energy trading in a community microgrid," in *Proc. IEEE Power Energy Soc. Gen. Meeting*, Chicago, IL, USA, Jul. 2017, pp. 1–5.

[16] P. Baez-Gonzalez, E. Rodriguez-Diaz, J. C. Vasquez, and J. M. Guerrero, "Peer-to-peer energy market for community microgrids [Technology Leaders]," *IEEE Electrific. Mag.*, vol. 6, no. 4, pp. 102–107, Dec. 2018.

[17] N. Liu, X. Yu, C. Wang, C. Li, L. Ma, and J. Lei, "Energy-sharing model with price-based demand response for microgrids of peer-to-peer prosumers," *IEEE Trans. Power Syst.*, vol. 32, no. 5, pp. 3569–3583, Sep. 2017, doi: 10.1109/TPWRS.2017.2649558.

[18] D. J. Vergados, I. Mamounakis, P. Makris, and E. Varvarigos, "Prosumer clustering into virtual microgrids for cost reduction in renewable energy trading markets," *Sustain. Energy, Grids Netw.*, vol. 7, pp. 90–103, Sep. 2016, doi: 10.1016/j.segan.2016.06.002.

[19] R. Carli, M. Dotoli, and R. Pellegrino, "A hierarchical decision-making strategy for the energy management of smart cities," *IEEE Trans. Autom. Sci. Eng.*, vol. 14, no. 2, pp. 505–523, Apr. 2017, doi: 10.1109/TASE.2016.2593101.

[20] A. Paudel, K. Chaudhari, C. Long, and H. B. Gooi, "Peer-to-peer energy trading in a prosumer-based community microgrid: A game-theoretic model," *IEEE Trans. Ind. Electron.*, vol. 66, no. 8, pp. 6087–6097, Aug. 2019, doi: 10.1109/TIE.2018.2874578.

[21] Z. Su, Y. Wang, Q. Xu, M. Fei, Y.-C. Tian, and N. Zhang, "A secure charging scheme for electric vehicles with smart communities in energy blockchain," *IEEE Internet Things J.*, vol. 6, no. 3, pp. 4601–4613, Jun. 2019, doi: 10.1109/JIOT.2018.2869297.

[22] B. C. Neagu, G. Grigoras, and O. Ivanov, "An efficient peer-to-peer based blokchain approach for prosumers energy trading in microgrids," in *Proc. 8th Int. Conf. Modern Power Syst. (MPS)*, Cluj Napoca, Romania, May 2019, pp. 1–4.

[23] A. Paudel and G. H. Beng, "A hierarchical peer-to-peer energy trading in community microgrid distribution systems," in *Proc. IEEE Power Energy Soc. Gen. Meeting (PESGM)*, Portland, OR, USA, Aug. 2018, pp. 1–5.

[24] X. Hou, Y. Sun, J. Lu, X. Zhang, L. H. Koh, M. Su, and J. M. Guerrero, "Distributed hierarchical control of AC microgrid operating in grid-connected, islanded and their transition modes," *IEEE Access*, vol. 6, pp. 77388–77401, 2018, doi: 10.1109/ACCESS.2018.2882678.

[25] J. Rocabert, A. Luna, F. Blaabjerg, and P. Rodríguez, "Control of power converters in AC microgrids," *IEEE Trans. Power Electron.*, vol. 27, no. 11, pp. 4734–4749, Nov. 2012, doi: 10.1109/TPEL.2012.2199334.

[26] J. A. Ramos-Ruiz, P. Enjeti, and L. Xie, "Peer-to-peer energy transaction in microgrids with power electronics enabled angle droop control," in *Proc. IEEE Electron. Power Grid (eGrid)*, Charleston, SC, USA, Nov. 2018, pp. 1–6.

[27] Y. Khayat, Q. Shafiee, R. Heydari, M. Naderi, T. Dragicevic, J. W. Simpson-Porco, F. Dorfler, M. Fathi, F. Blaabjerg, J. M. Guerrero, and H. Bevrani, "On the secondary control architectures of AC microgrids: An overview," *IEEE Trans. Power Electron.*, vol. 35, no. 6, pp. 6482–6500, Jun. 2020, doi: 10.1109/TPEL.2019.2951694.

[28] M. M. A. Abdelaziz, H. E. Farag, E. F. El-Saadany, and Y. A. I. Mohamed, "A novel and generalized three-phase power flow algorithm for islanded microgrids using a Newton trust region method," *IEEE Trans. Power Syst.*, vol. 28, no. 1, pp. 190–201, Feb. 2013, doi: 10.1109/TPWRS.2012.2195785.

[29] T. Shu, X. Lin, J. Tang, J. Yang, F. Liu, J. Zheng, and S. Peng, "Power flow analysis for hybrid AC/DC microgrid islanding operation based on an improved adaptive droop control," in *Proc. 2nd IEEE Conf. Energy Internet Energy Syst. Integr. (EI2)*, Beijing, China, Oct. 2018, pp. 1–6.

[30] X. Yang, Y. Du, J. Su, X. Chen, and L. Chang, "An optimal secondary voltage control strategy for islanded microgrid," in *Proc. IEEE 8th Int. Power Electron. Motion Control Conf. (IPEMC-ECCE Asia)*, Hefei, China, May 2016, pp. 2880–2885.

[31] K. Hashmi, M. M. Khan, J. Xu, M. U. Shahid, S. Habib, M. T. Faiz, and H. Tang, "A quasi-average estimation aided hierarchical control scheme for power electronics-based islanded microgrids," *Electronics*, vol. 8, pp. 39–68, Jan. 2019, doi: 10.3390/electronics8010039.

[32] E. González-Romera, E. Romero-Cadaval, C. Roncero-Clemente, M. Ruiz-Cortés, F. Barrero-González, M. I. Milanés-Montero, and A. Moreno-Muñoz, "Secondary control for storage power converters in isolated nanogrids to allow peer-to-peer power sharing," *Electronics*, vol. 9, pp. 140–157, Jan. 2020, doi: 10.3390/electronics9010140.

[33] C. Roncero-Clemente, N. Vilhena, V. Delgado-Gomes, E. Romero-Cadaval, and J. F. Martins, "Control and operation of a three-phase local energy router for prosumers in a smart community," *IET Renew. Power Gener.*, vol. 14, no. 4, pp. 560–570, Mar. 2020, doi: 10.1049/iet-rpg.2019.0589.

[34] Y. Liu, Z. Qu, H. Xin, and D. Gan, "Distributed real-time optimal power flow control in smart grid," *IEEE Trans. Power Syst.*, vol. 32, no. 5, pp. 3403–3414, Sep. 2017, doi: 10.1109/TPWRS.2016.2635683.

[35] W. Price, "Bibliography on load models for power flow and dynamic performance simulation," *IEEE Trans. Power Syst.*, vol. 10, no. 1, pp. 523–538, Feb. 1995, doi: 10.1109/59.373979.

[36] N. Ghanbari and S. Bhattacharya, "SoC balancing of different energy storage systems in DC microgrids using modified droop control," in *Proc. 44th Annu. Conf. IEEE Ind. Electron. Soc.*, Washington, DC, USA, Oct. 2018, pp. 6094–6099.

[37] Spanish Ministry of Economy. *Royal Decree 1955/2000 of 1 December, Which Regulates the Activities of Transmission, Distribution, Marketing, Supply and Installations of Electricity Authorization Procedures*. Accessed: Nov. 19, 2020. [Online]. Available: https://www.boe.es/buscar/pdf/2000/BOE-A-2000-24019-consolidado.pdf

[38] E. Makovenko, O. Husev, J. Zakis, C. Roncero-Clemente, E. Romero-Cadaval, and D. Vinnikov, "Passive power decoupling approach for three-level single-phase impedance source inverter based on resonant and PID controllers," in *Proc. 11th IEEE Int. Conf. Compat., Power Electron. Power Eng. (CPE-POWERENG)*, Cadiz, Spain, 2017, pp. 516–521.

[39] M. Karimi-Ghartemani, S. A. Khajehoddin, P. Jain, and A. Bakhshai, "A systematic approach to DC-bus control design in single-phase grid-connected renewable converters," *IEEE Trans. Power Electron.*, vol. 28, no. 7, pp. 3158–3166, Jul. 2013, doi: 10.1109/TPEL.2012.2222672.

[40] M. Merai, M. W. Naouar, I. Slama-Belkhodja, and E. Monmasson, "An adaptive PI controller design for DC-link voltage control of single-phase grid-connected converters," *IEEE Trans. Ind. Electron.*, vol. 66, no. 8, pp. 6241–6249, Aug. 2019, doi: 10.1109/TIE.2018.2871796.

CARLOS RONCERO-CLEMENTE received the international Ph.D. degree in electrical, electronic and control engineering from the University of Extremadura, Spain, in 2016. During his Ph.D. research, he was a Visiting Student with the Tallinn University of Technology and Aalborg University. He was a Postdoctoral Researcher with the Nova University of Lisbon from 2016 to 2019. He is currently a Senior Researcher in power electronic and renewable energies with the University of Extremadura. His research interests include power electronic topologies and controls for renewable energy applications and smart grids. He is author of more than 30 journal papers and 75 international conferences.

EVA GONZÁLEZ-ROMERA received the M.Sc. degree in industrial engineering and the Ph.D. degree in electrical engineering from the University of Extremadura, Badajoz, Spain, in 1998 and 2005, respectively. She is currently a Professor with the Department of Electrical Engineering, Electronics, and Control, and belongs to the Research Group in Power Electrical and Electronic Systems (PE&ES), University of Extremadura. Her primary areas of interest are power quality, distribution grids, and smart grids. She has coordinated research projects about load forecasting, integration of photovoltaic power plants in distribution networks, and control of nanogrid.

FERMÍN BARRERO-GONZÁLEZ (Senior Member, IEEE) received the M.Sc. degree in electrical engineering from the Universidad Politécnica de Madrid, Madrid, Spain, in 1984, and the Ph.D. degree in electrical and electronic engineering from the Universidad Nacional de Educación a Distancia, Madrid, in 1995. He is currently a Professor of electrical engineering with the Universidad de Extremadura, Badajoz, Spain, where he is currently coordinating the Power Electrical and Electronic Systems Research Group. His research interest areas are power electronics in the power systems, flexible ac transmission systems, active power filters, and electrical machine drives.

MARÍA ISABEL MILANÉS-MONTERO (Member, IEEE) received the M.Sc. degree in industrial engineering and the Ph.D. degree in electrical and electronic engineering from the University of Extremadura, Spain, in 1997 and 2005, respectively. In November 1998, she joined the School of Industrial Engineering, University of Extremadura, as an Assistant Professor and a Researcher with the Power Electrical and Electronic Systems Research and Development Group. Her major fields of expertise include power quality, renewable energy sources control, energy storage management systems, smart grids, and electric vehicles.

ENRIQUE ROMERO-CADAVAL (Senior Member, IEEE) received the M.Sc. degree in industrial electronic engineering from the Universidad Pontificia de Comillas, Madrid, Spain, in 1992, and the Ph.D. degree in electrical and electronic engineering from the Universidad de Extremadura, Badajoz, Spain, in 2004. In 1995, he joined the University of Extremadura, where he is a Professor of power electronics and a Researcher with the Power Electrical and Electronic Systems Research and Development Group, School of Industrial Engineering. His research interests are power electronics applied to power systems, power quality, active power filters, electric vehicles, smart grids, and control and integration into the grid of distributed/renewable energy resources.

• • •